

Aminotetrazole-Functionalized SiO_2 Coated MgO Nanoparticle Composites for Removal of Acid Fuchsin Dye and Detection of Heavy Metal Ions

Sarathkumar Krishnan, Sobhan Chatterjee, Ankit Solanki, Nikita Guha, Mayank K. Singh, Anoop K. Gupta, and Dhirendra K. Rai*



Cite This: *ACS Appl. Nano Mater.* 2020, 3, 11203–11216



Read Online

ACCESS |

Metrics & More

Article Recommendations

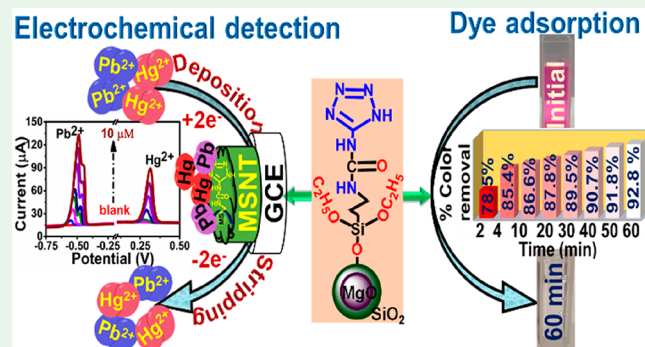
Supporting Information

ABSTRACT: Stepwise synthesis of aminotetrazole functionalized $\text{MgO}-\text{SiO}_2$ (MSNT) nanocomposites has been achieved by a simple wet chemical method. The as-synthesized nanomaterial is investigated for the removal of dye and the detection of heavy metal ions from the aqueous solutions. The structural, textural, and morphological characteristics of the nanocomposites are characterized by P-XRD, FT-IR, solid-state NMR, TGA, BET N_2 isotherm, FE-SEM, and TEM techniques. The dye adsorption studies reveal that the material selectively and rapidly adsorbs the acid fuchsin (AF) dye (78% color removal within 2 min) with high adsorption capacity (775.6 mg/g) and good recyclability. The adsorption isotherm and kinetic studies indicate that the dye adsorption takes place by the Freundlich isotherm and pseudo-second-order kinetic model. The material has been used to modify the glassy carbon electrode (GCE) for the detection of $\text{Pb}(\text{II})$ and $\text{Hg}(\text{II})$ ions by square wave anodic stripping voltammetry (SWASV), which shows excellent sensitivity ($\approx 75 \mu\text{A}\cdot\mu\text{M}^{-1}\cdot\text{cm}^{-2}$ and $40 \mu\text{A}\cdot\mu\text{M}^{-1}\cdot\text{cm}^{-2}$) and low detection limit (0.019 μM and 0.041 μM) for $\text{Pb}(\text{II})$ and $\text{Hg}(\text{II})$ ions, respectively. The practical applicability of the material for heavy metal ion detection has also been ascertained by stability, reproducibility, interference, simultaneous detection, and real-time sample studies.

KEYWORDS: hybrid materials, surface functionalization, dye removal, heavy metal ion sensing, electrochemical stripping analysis

1. INTRODUCTION

The increasing discharge of effluents contaminated with toxic organic dyes and heavy metal ions (HMIs) from various industries (textile, food processing, cosmetics, chemical fertilizer, pesticide, pharmaceutical, and plastic industries) is posing many environmental challenges.^{1,2} Due to their nonbiodegradable nature, the accumulation of toxic organic dyes and HMIs ($\text{Hg}(\text{II})$, $\text{Pb}(\text{II})$, $\text{Cu}(\text{II})$, $\text{Cd}(\text{II})$) in the food cycle has become one of the significant health concerns.^{3–5} Several international agencies, such as World Health Organisation (WHO), Centre for Disease Control (CDC), Joint Food and Agricultural Organization (FAO), and International Agency for Research on Cancer (IARC), have recommended an optimum level of the heavy metal ions in the ecosystem, beyond which they could lead to several irreversible changes in the environment and human life.⁵ Therefore, the design and synthesis of new sustainable materials for the removal of dye contaminants and the reliable and sensitive detection of heavy metal ions from the aqueous systems have become essential research areas.

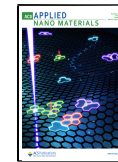


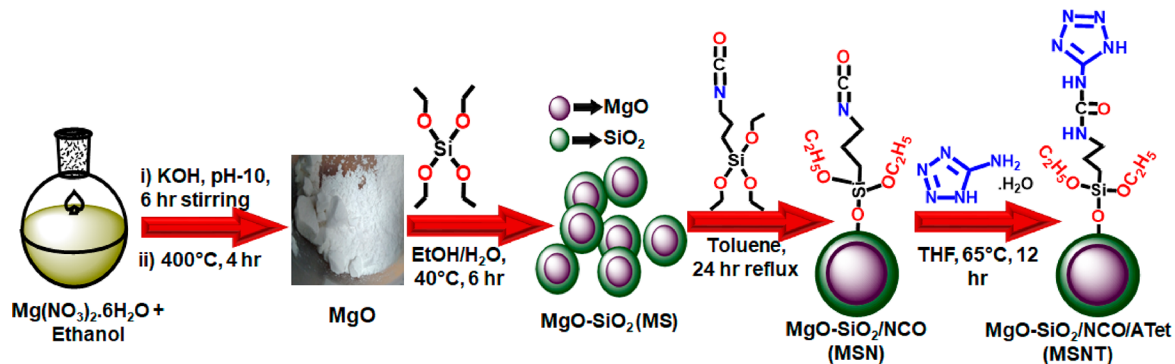
For dye removal, among the various techniques employed, such as biological treatment, chemical oxidation, coagulation and flocculation, membrane separation, photocatalytic degradation, and adsorption,^{6,7} adsorption is the most preferred method because of its low cost, smooth operation, and less energy consumption.^{6,8} Thus, the development of solid adsorbents for adsorption has garnered a tremendous interest. For HMI detection, several analytical techniques, such as fluorescence spectroscopy, atomic absorption spectroscopy, inductively coupled plasma mass spectroscopy, and atomic emission spectroscopy, have been used.⁹ However, complexity in handling and sample preparation, costly experiments, and time-consuming process impede the heavy metal ion detection by these techniques.¹⁰ Among the other methods, electro-

Received: August 29, 2020

Accepted: October 26, 2020

Published: November 9, 2020



Scheme 1. Diagram of the Synthesis of MgO–SiO₂/NCO/ATet Hybrid Material

chemical stripping voltammetry has gained considerable interest due to its easy handling, low-cost instrumentation, and highly sensitive and selective analysis.¹¹

So far, various solid adsorbents, including metal oxides, carbon-based materials, inorganic–organic hybrid materials (IOHMs), metal–organic frameworks, have been used for dye removal and HMI sensing.^{12–14} Notably, besides having a large surface area and tunable pore structure,¹⁵ IOHMs offer additional active sites for the dye adsorption and heavy metal ion sensing compared to other materials due to the synergistic effect of inorganic and organic components.^{16–18} The inorganic solid support plays a crucial role in maintaining thermal stability and structural order. At the same time, the organic functionalization provides tunable porosity and, thereby, offers superior adsorption capacity with better selectivity and sensitivity.^{15,16,19} Owing to these physicochemical properties, IOHMs have drawn tremendous interest for dye adsorption, detection of heavy metal ions, catalysis, energy storage devices, gas adsorption, and separation.^{16,17,20,21} For IOHM fabrication, nowadays, silica-coated magnesium oxide (MgO-SiO_2) nanocomposite has become a preferred choice as inorganic solid support because of natural abundance, less toxicity, large surface area, and higher thermal tolerance of the silica component.^{22,23} The use of MgO nanoparticles (NPs) improves and maintains the basicity of the overall system so that the performance level is not sacrificed. Moreover, the charged surface of MgO (isoelectric point 12.4) also plays an important role in the adsorption processes governed by electrostatic interactions.²²

For organic functionalization, nitrogen-rich organic moieties, particularly aliphatic and aromatic amines, have been extensively explored to facilitate dye adsorption and HMI detection, mainly because of their H-bonding and metal coordination abilities, respectively. For example, Aoopngan et al. reported the synthesis of MgFe_2O_4 nanoparticles, which, upon functionalization with ethanolamine, showed better adsorption capacity for congo red dye adsorption due to the electrostatic attraction between surface amine groups and dye molecules.¹⁷ A polyaniline/single-wall carbon nanotube (PANI/SWCNT) composite modified by ethylenediamine-tetraacetic acid (EDTA) exhibited superior selectivity for the electrochemical detection of $\text{Cu}(\text{II})$, $\text{Pb}(\text{II})$, and $\text{Hg}(\text{II})$ ions. Also, it increased the sensitivity by offering the roughness to the electrode surface, thereby increasing the effective surface area.²⁴ The chelation characteristics of amino acid cysteine have also been explored in surface functionalization of materials to fabricate better electrochemical sensors.¹⁶

In this report, we have stepwise synthesized the MgO-SiO_2 –tetrazole nanocomposite by simple precipitation and reflux method and studied its dual-functional applications in AF dye removal as well as in electrochemical sensing of Pb^{2+} and Hg^{2+} ions. Acid fuchsin (AF) dye is an anionic dye consisting of a highly conjugated triphenylmethane framework. It is widely used for dyeing textile fabrics, pesticide synthesis, and biological staining.. Its high toxicity and tenacity cause carcinogenic and mutagenic effects on humans and detrimentally impact the environment, which mandate the removal of AF dye contamination from wastewater.²⁵ The consideration of 5-aminotetrazole (having five N atoms) as our surface functionalization agent is based on the aforementioned fact that the N-rich organic surface modifiers have been established to augment the adsorption capacity as well as selectivity in dye adsorption and HMI detection. Although surface functionalization by several aliphatic and aromatic amines (amidogen,²⁶ ethanolamine,¹⁷ polyethylenimine,^{24,27} 1,6-hexanediamine,²⁸ polylysine-chitosan,^{29,30} (3-aminopropyl)triethoxysilane,^{31,32} thiourea appended 1,8-naphthalimide,³³ dopamine,³⁴ triazine,³⁵ and phenylamine³⁶) has been extensively used in dye adsorption and HMI detection, aminotetrazole has not been employed as surface functionalization agent for these applications to the best of our knowledge. However, there are reports where 5-aminotetrazole has been used as a linker for the synthesis of nitrogenous MOFs for CO_2 capture.³⁷ Our results reveal that the as-prepared inorganic–organic hybrid nanomaterial shows selective high adsorption capacity with good regeneration capability for anionic acid fuchsin (AF) dye. The material also exhibits excellent sensitivity for electrochemical detection of $\text{Pb}(\text{II})$ and $\text{Hg}(\text{II})$ ions without any considerable interference, even in their real-time samples. The detailed studies of adsorption mechanism, kinetics, and isotherms have also been discussed. To the best of our knowledge, this is the first effort to investigate a porous hybrid amine-based nanomaterial for the rapid and selective dye adsorption as well as for sensitive detection of heavy metal ions.

2. EXPERIMENTAL SECTION

2.1. Materials. All the reagents and solvents were used as received without further purification. Magnesium nitrate ($\text{Mg}(\text{NO}_3)_2 \cdot 6\text{H}_2\text{O}$) and potassium hydroxide were purchased from ADVENT ChemBio PVT. Ltd. Tetraethyl orthosilicate (TEOS) and 3-(triethoxysilyl)-propyl isocyanate (TESPIC) were purchased from TCI Chemicals. 25% Ammonia solution, toluene, tetrahydrofuran (THF), and 5-aminotetrazole monohydrate (ATet) were purchased from Spectrochem Pvt. Ltd. Ethanol was purchased from Changshu Hongsheng

Fine Chemicals, and Millipore water was used throughout the experiment.

2.2. Preparation of MgO Nanoparticles. The MgO nanoparticles were synthesized by a simple precipitation method, as shown in Scheme 1. 10 g of $\text{Mg}(\text{NO}_3)_2 \cdot 6\text{H}_2\text{O}$ was dissolved in 20 mL of ethanol, and the mixture was magnetically stirred in a 250 mL round-bottom flask for 15 min. The pH was adjusted to 10 through the addition of potassium hydroxide in the mixture. The reaction was kept at 70 °C for 6 h. The obtained suspension was filtered and washed three times with water and ethanol using a suction flask. The resulting precipitate was kept in a vacuum oven overnight at 80 °C and subsequently calcined at 500 °C for 2 h.

2.3. Functionalization of Silica onto MgO NPs. The as-prepared MgO (3.0 g) was suspended in an RB flask containing 80 mL of ethanol and 20 mL of water by ultrasonication for 15 min, followed by continuous stirring. After stirring for 15 min, 6 mL of 25% ammonia solution and 6 mL of TEOS were added dropwise, and the reaction mixture was continuously stirred for 6 h at 40 °C. The resultant reaction mixture was washed three times with water and ethanol and dried at 80 °C overnight in vacuo to obtain dry MgO-SiO_2 (MS).

2.4. Grafting of MgO-SiO_2 with 3-(Triethoxysilyl)propyl Isocyanate. The chemical grafting of 3-(triethoxysilyl)propyl isocyanate on MgO-SiO_2 was done using previously reported methodology.³⁸ In this process, 2.25 g of MgO-SiO_2 precursor was added to 20 mL of toluene. To this stirring suspension, 2.25 mL of TEPSIC was added dropwise, and the reaction mixture was refluxed for 24 h under N_2 atmosphere. Afterward, the TEPSIC grafted MgO-SiO_2 (MSN) was washed repeatedly with toluene and ethanol and was dried in a vacuum oven overnight at 80 °C.

2.5. Surface Modification by 5-Aminotetrazole. Covalent linkage of 5-aminotetrazole to as-synthesized MSN was achieved following the reported procedure.^{38,39} In this procedure, 1.7 g of as prepared MSN and 1 g of 5-aminotetrazole monohydrate were added in 20 mL of THF, and the suspension was stirred for 12 h at 65 °C under nitrogen atmosphere. After completion of the reaction, the reaction mixture was filtered and thoroughly washed with THF and ethanol. The obtained MgO-SiO_2 -TEPSIC-ATet (MSNT) nanocomposite was dried in a vacuum oven for 8 h.

2.6. Structural Characterization. The structural confirmation of the as-synthesized materials was investigated through powder X-ray diffraction (PXRD) measurement using X-ray diffractometer (Rigaku, Ultima VI) with $\text{Cu K}\alpha$ radiation ($\lambda = 1.54 \text{ \AA}$) in the 2θ range of 10°–80° with a step size of 0.02°. Fourier transform infrared spectroscopy (FT-IR) spectra were recorded on an FTIR spectrometer (Bruker Tensor 27) in the wavelength range 400 cm^{-1} to 4000 cm^{-1} . Thermogravimetric analyses (Netzsch, TG 209 Tarsus) were carried out from 30° to 800 °C under nitrogen atmosphere at the heating rate of 10 °C/min. Solid-state ^{13}C cross-polarization magic angle spinning (CP-MAS) NMR spectra were obtained using a BRUKER Advance II 400 MHz spectrometer with a 4 mm MAS probe.

The surface morphologies of as-synthesized NPs were examined by field emission scanning electron microscopy (FE-SEM) system (JEOL, 7610F Plus) with an acceleration voltage of 5 kV. Before the FE-SEM analysis, the samples were coated with a gold conductive coating. The elemental composition was measured with an energy dispersive X-ray spectroscopy (EDX) detector integrated with the FE-SEM instrument. Transmission electron microscopy (TEM) images were recorded on FEI, TECNAI G2 TEM microscope with an operating voltage of 200 kV. The textural properties of as-synthesized materials were characterized by Autosorb iQ3 (Quantachrome) gas sorption analyzer under N_2 adsorption at 77 K. Prior to the adsorption studies, the samples were degassed at 105 °C for 8 h in a vacuum. The specific surface area and pore size distribution were calculated using the Brunauer–Emmett–Teller (BET) method in the relative pressure range of 0.05 to 1.00 bar and Barrett–Joyner–Halenda (BJH) method, respectively. The surface area was calculated from the adsorption branches of the isotherm in the relative pressure (P/P_0) range 0.05 to 0.30. The pore size distributions were

investigated using desorption branches of the isotherm. The pore volume was calculated at a relative pressure of 0.98. The ζ potential measurements were carried out using Horiba SZ-100 nanoparticle analyzer. Residual concentrations after the dye adsorption studies were determined by Shimadzu 2400 UV-vis spectrometer.

2.7. Dye Adsorption Experiments. **2.7.1. Measurement of Concentration-Dependent Adsorption Capacity (Q_e).** Adsorption study of acid fuchsin (AF) dye, from aqueous solutions of varying concentrations (20, 40, 60, 60, 100, 120, 150 mg/L), using MSNT, was evaluated by batch adsorption experiments at pH 5–6. The effect of pH on color removal efficiency was investigated at various pH values ranging from 3.0 to 9.0. The pH of the dye solutions was adjusted using 0.1 M HNO_3 and 0.1 M NaOH solutions, and the unknown concentrations were evaluated by UV-vis spectroscopy (Shimadzu 2400). Each adsorption experiment was carried out in a 50 mL centrifuge tube, which was stirred for 5 min with 5 mg of MSNT at 250 rpm using a Abdos E11231 digital stirrer, after which kept at the static condition for 4 h to achieve the adsorption equilibrium. Afterward, the filtrate from each batch was centrifuged at 5000 rpm, and subsequently, the UV-vis spectrum was recorded. The percentage (%) of color removal and adsorption capacity for each batch was calculated from the following equations,⁴

$$\% \text{ color removal} = \frac{C_0 - C_e}{C_0} \times 100 \quad (1)$$

$$\text{adsorption capacity } Q_e = \frac{(C_0 - C_e)V}{W} \quad (2)$$

where Q_e is the adsorption capacity (mg/g) and C_0 and C_e are the initial and equilibrium concentrations (mg/L) of AF dye, respectively. V and W are the solution volume (50 mL) and the mass of the adsorbent (5 mg), respectively.

2.7.2. Measurement of Time-Dependent Adsorption Capacity (Q_t). In this study, adsorption of 50 mL of dye solution of concentration 20 mg/L was allowed on 5 mg of MSNT in a 100 mL conical flask. Time-dependent adsorption capacities (Q_t) were calculated by recording UV-vis spectra of the fraction of filtrate in the time intervals of 0, 2, 4, 10, 20, 30, 40, 50, and 60 min using the following equation,¹⁷

$$\text{adsorption capacity } Q_t = \frac{(C_0 - C_t)V}{W} \quad (3)$$

where Q_t is the adsorption capacity (mg/g) at time t , C_0 is the initial concentration (20 mg/L), and C_t is the equilibrium concentration (mg/L) of AF dye at time t .

2.7.3. Recyclability Experiments. The recyclability of MSNT for dye adsorption was studied by performing five cycles of the adsorption–desorption experimentation. By use of eq 1, the percentage color removal ability of the material was calculated by UV-vis spectroscopy after the adsorption in each cycle. In the first cycle, adsorption of 50 mL of AF dye aqueous solution of concentration 20 mg/L was stirred with 5 mg of MSNT at 250 rpm, and then the suspension was kept at the static condition for 4 h to achieve the adsorption equilibrium. Afterward, the suspension was centrifuged at 5000 rpm for 2 min to allow the dye adsorbed MSNT (MSNT@AF) to settle. The filtrate was removed and subjected to UV-vis spectroscopy. The desorption of AF from MSNT@AF was achieved by stirring MSNT@AF in 25 mL of 6 M NaCl solution for 30 min at room temperature.⁷ The suspension was again centrifuged at 5000 rpm for 2 min, and the red colored filtrate was removed. The obtained MSNT was again centrifuged in deionized water and dried in a vacuum oven for 6 h at 80 °C. Following similar steps, the dried MSNT was further subjected to four more adsorption–desorption cycles, and the percentage color removal ability was calculated for each cycle using eq 1.

2.8. Electrochemical Sensing. **2.8.1. Modification of the Working Electrode and Electrochemical Detection of HMs.** Square wave anodic stripping voltammetry (SWASV) experiments were recorded on a AUTOLAB PGSTAT 204 potentiostat using a three-

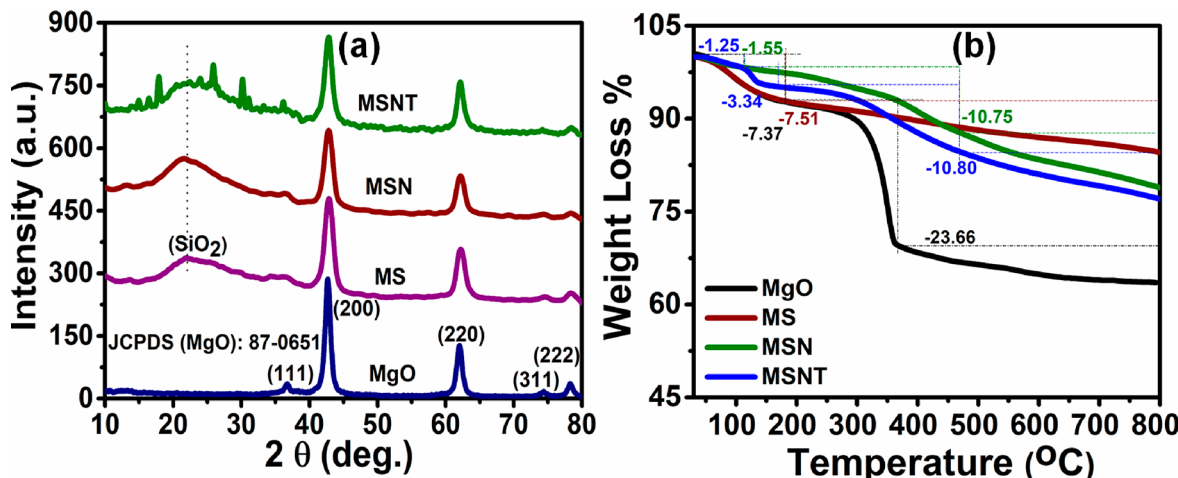


Figure 1. (a) P-XRD spectra and (b) TGA spectra of the MgO, MS, MSN, and MSNT.

electrode system (5 mm glassy carbon electrode (GCE) as a working electrode, platinum (Pt) as an auxiliary electrode, and Ag/AgCl (saturated with KCl) as a reference electrode). Before the modification, the GC electrode was polished with 0.5 μm alumina powder and rinsed with ultrapure water. Subsequently, it was sonicated in ethanol and ultrapure water and dried at room temperature. For drop-casting, three separate suspensions were prepared by dispersing 10 mg of MgO, MS, and MSNT in 1 mL of ethanol by sonication for 30 min. To prepare modified GC electrodes (GC-MgO, GC-MS, and GC-MSNT), an amount of 10 μL of as-prepared suspensions of MgO, MS, and MSNT was drop casted on the active area of the GC working electrodes and dried at room temperature. All the electrochemical measurements were carried out using a 0.1 M acetate buffer (NaAc–HAc) solution with pH 5.0, deposition time of 120 s, deposition potential of -1 V, and the pulse amplitude of 50 mV. The repeatability, reproducibility, stability, interference, and real-time sample studies were carried out with 40 mL of 20 μM analyte solutions.

2.8.2. Real-Time Sample Analysis. For real-time sample analysis, tap and pond water samples were collected from the local body and were filtered using a filter membrane (2.5 μm). The resulting filtrates were diluted with 0.1 M NaAc–HAc buffer solution (pH 5.0) in a volume ratio of 1:9. The stripping current response of 40 mL of each diluted solution was recorded, which was designated as i_{unspiked} . To this unspiked sample, 4 μL of 0.2 M analyte solution was added, and the stripping current was recorded, which was designated as i_{spiked} . The % recovery (% R) was calculated using the following equation:^{14,40}

$$\% R = \frac{(i_{\text{spiked}} - i_{\text{unspiked}})}{i_{\text{known}}} \times 100 \quad (4)$$

The parameter i_{known} represents the stripping current from the calibration plot corresponding to 20 μM concentration of the analyte. Each measurement was performed three times to calculate the standard deviation.

3. RESULTS AND DISCUSSION

3.1. Synthesis and Materials Characterization. To facilitate the rapid adsorption of dye and selective detection of heavy metal ions, modification of solid material with suitable functionality is the desired process. In this regard, the synthesis of aminotetrazole functionalized nanomaterial MgO–SiO₂–(CH₂)₃–NHCONH–Tet (MSNT) was achieved via syntheses of intermediate materials; MgO, MgO–SiO₂ (MS), and MgO–SiO₂–(CH₂)₃–NCO (MSN), as depicted in Scheme 1. The synthesis of MS was achieved by the reaction of MgO

nano-particles, obtained through precipitation of Mg(NO₃)₂·6H₂O under basic conditions, with TEOS. The subsequent chemical modification of the silica pores of MS by TEPSIC led to the formation of MSN, containing free –NCO groups covering the SiO₂ pore wall. The free –NCO groups of MS were further explored to link the nitrogen-rich aminotetrazole to obtain the final material MSNT by the reaction of MSN with hydrated 5-aminotetrazole. In the final material MSNT, the presence of carbamide and tetrazole moieties in the pores of mesoporous silica is expected to enhance the dye adsorption capacity and selective HMI sensing through H-bonding and nitrogen lone pair coordination, respectively. Moreover, the C₃ aliphatic linker is known to increase the hydrophobicity of the material,^{41,42} which facilitates the preferential adsorption of organic dye on the surface of MSNT.

The structural characterizations of as-synthesized materials (MgO, MS, MSN, and MSNT) were done by P-XRD analysis. The diffraction pattern of pristine MgO (Figure 1a) shows the characteristic diffraction from (111), (200), (220), (222), and (311) planes of a phase pure cubic crystalline MgO (JCPDS: 87-0651).⁴³ In the case of MS, silica functionalization leads to the appearance of an additional broad peak, having amorphous characteristics, in the 2θ range of 15–30°, while no change in the position of MgO peaks was observed. After the chemical grafting of TEPSIC on MS, no new phase was detected in the diffraction pattern of MSN. However, a slight decrease in the peak intensities was observed due to the coverage of TEPSIC on the MS surface.⁴⁴ In the final material MSNT, the overall P-XRD pattern remains the same; however, some peaks in the 2θ range of 15–36° can be attributed to the functionalization of aminotetrazole groups on MSN.⁴⁵ From the P-XRD patterns of all the four materials, it is evident that during the successive functionalization of MgO, the structural integrity of crystalline MgO remains unaltered.

The thermal stability and the degree of functionalization of the as-prepared materials were investigated using thermogravimetric analyses, which are depicted in Figure 1b. The TGA curve of MgO shows two-step dehydration in the range of 30–350 °C, corresponding to the desorption of the surface-bound water (7.37%) and the dehydroxylation process (23.66%).⁴⁶ In the case of MS, only one weight loss step (30–180 °C, 7.51%), related to dehydration of physically adsorbed water molecules, can be seen. For MSN and MSNT, besides dehydration weight losses (30–115 °C; 1.55% (MSN), 1.25% (MSNT)), the

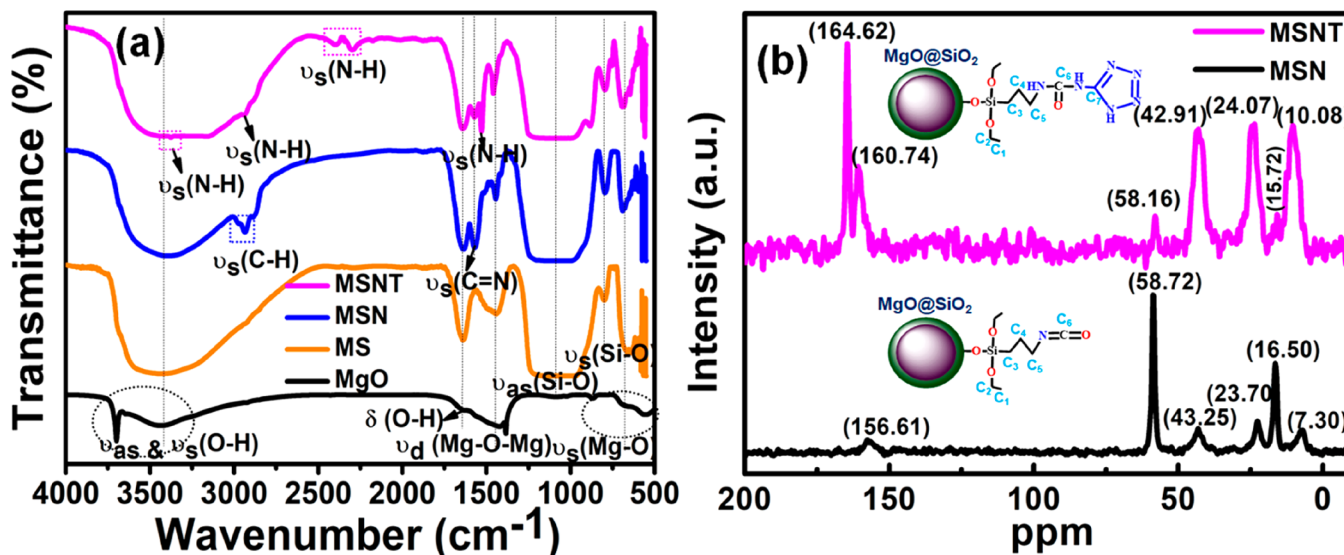


Figure 2. (a) FT-IR spectra of **MgO**, **MS**, **MSN**, and **MSNT** and (b) solid-state NMR spectra of **MSN** and **MSNT**.

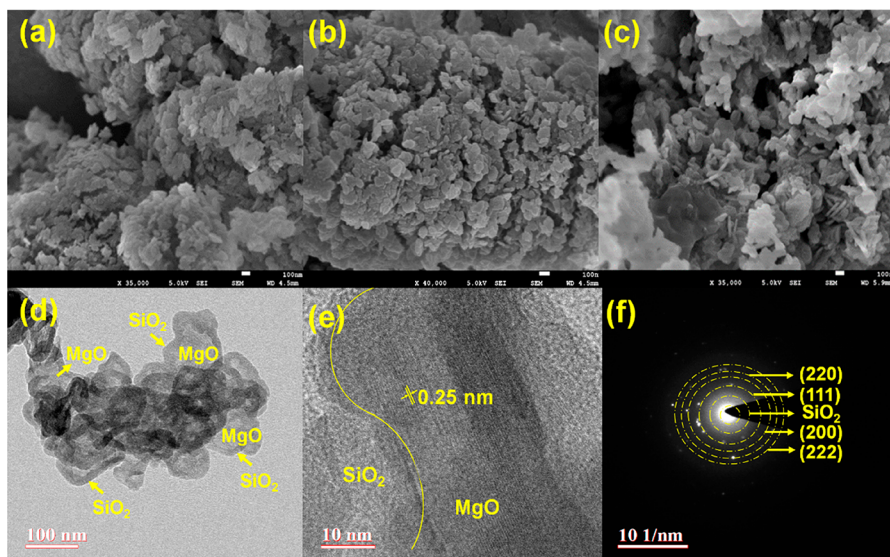


Figure 3. FE-SEM of (a) **MgO**, (b) **MS**, and (c) **MSNT** and (d) TEM, (e) HRTEM, and (f) SAED pattern of **MSNT**.

second weight-loss region (115–470 °C) is assigned to the loss of organic functional groups of the materials. In the second region, **MSNT** shows two weight losses (3.34% and 10.80%) compared to only one weight loss in **MSN** (10.75%), indicating one- and two-step organic functionalization in **MSN** and **MSNT**, respectively. Overall, TGA supports the expected degree of functionalization and also shows good stability of the material up to 115 °C. Results from comparison of % weight loss values of the as-prepared materials and their corresponding regions are tabulated in Table S1.

The FT-IR spectra of the materials were recorded to study the presence of the surface functional groups (Figure 2a). For **MgO**, besides peaks at 872, 680, and 550 cm^{-1} for Mg–O bond stretching and bending,⁴⁷ a broad Mg–O–Mg deformation band at 1450 cm^{-1} can also be seen in its FT-IR spectrum. Moreover, the appearance of bands at 1643, 3425, 3696 cm^{-1} can be attributed to bending and symmetrical and asymmetrical stretching vibrations of adsorbed water molecules, respectively. In the case of **MS**, the new peaks at

802 and 1087 cm^{-1} correspond to the bending and stretching vibration of the Si–O bond, respectively,²³ which confirm the formation of the **MgO–SiO₂** structure. In **MSN**, the chemical modification of **MgO–SiO₂** with TEPSIC leads to the appearance of new peaks representing $\nu_{\text{C}=\text{N}}$ (1569 cm^{-1}) and methylene ν_{CH_2} (2934 and 2980 cm^{-1}) groups of TEPSIC, suggesting chemical grafting of TEPSIC on **MS**. As compared to **MSN**, several new peaks, at 1532 cm^{-1} and in the region of 2200–3250 cm^{-1} , correspond to characteristic N–H bond vibrations of the aminotetrazole group.^{39,48} The broad nature of $\nu_{\text{O-H}}$ peak of adsorbed H_2O on **MSNT** obscures one of the $\nu_{\text{N-H}}$ peaks at 3377 cm^{-1} and makes it almost indiscernible. Overall, the FT-IR spectra of the four materials suggest the successful functionalization of aminotetrazole on the surface of **MS**.

To further confirm the chemical grafting of the organic isocyanate and aminotetrazole groups on the pore wall of mesoporous **MSN**, solid-state ^{13}C CP-MAS NMR spectra of **MSN** and **MSNT** were also recorded (Figure 2b). The ^{13}C

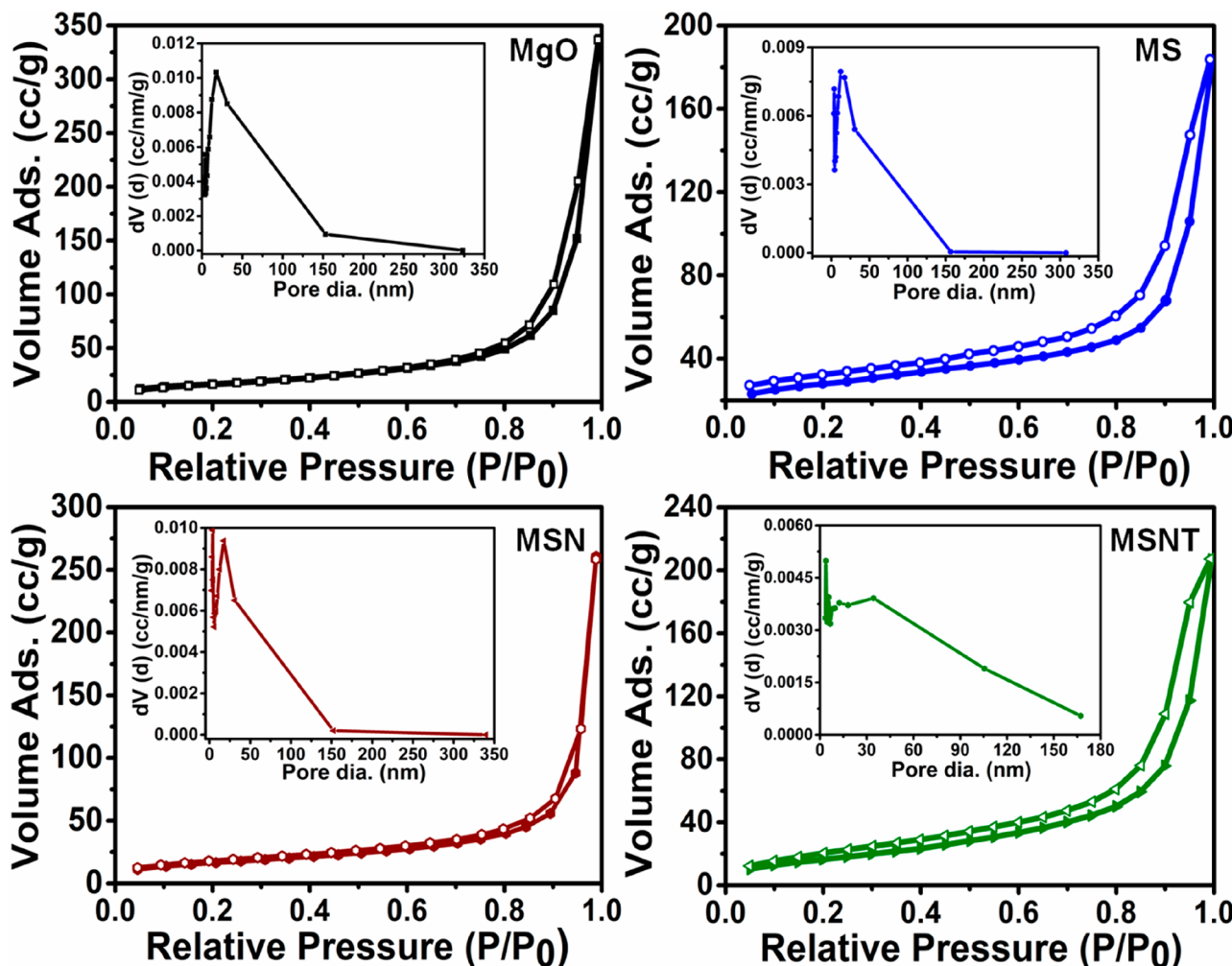


Figure 4. N_2 adsorption/desorption isotherm and pore size distribution of the as-prepared MgO, MS, MSN, and MSNT.

solid-state NMR of **MS** shows the resonance peaks for aliphatic carbons of the C_3 linker (16.50, 23.70, and 43.25 ppm) as well as for some free ethoxy groups (7.30 and 58.72 ppm) of TEPSIC besides its carbamide carbon at 156.61 ppm.⁴⁹ In the case of **MSNT**, the same set of peaks appear at 15.27, 24.07, 42.91, 10.08, 58.16, and 160.74 ppm, respectively; however, an additional peak at 164.62 ppm for tetrazole ring carbon can also be seen.^{37,50} In the line of FT-IR, the solid-state ^{13}C CP-MAS NMR spectra of **MSN** and **MSNT** also confirm the successive chemical grafting of TEPSIC and aminotetrazole functionalities on the pore-lining of the mesoporous **MS** material.

The morphologies of the as-prepared materials were examined by FE-SEM and TEM analyses. Figure 3a–c shows the FE-SEM images of MgO, **MS**, and **MSNT**, respectively. The SEM image of MgO shows an irregular shaped, agglomerated, and poorly dispersed morphology; however, successive functionalization leads to a gradual dispersion of the constituent particles in **MS** and **MSNT**. SEM-EDX analysis of each material confirms the presence of corresponding elements in adequate proportion (Figure S1). Moreover, in the SEM elemental mapping of **MSNT** (Figure S2), a uniform distribution of constituent elements Mg, Si, O, C, and N can be seen, suggesting a uniform functionalization of organic groups throughout the pores of $\text{MgO}-\text{SiO}_2$. To further understand the structural details of the final **MSNT** material,

TEM analysis was carried out. The TEM image of **MSNT** (Figure 3d) displays two different contrast levels for MgO particles and SiO_2 components, indicating the successful MgO– SiO_2 composite structure. From high-resolution transmission electron microscopy (HRTEM), the interplanar lattice fringes of **MSNT** and its corresponding SAED pattern are depicted in Figure 3e and Figure 3f. The HR-TEM lattice fringes show an interplanar distance of 0.237 nm, which correlates to (111) diffraction planes of crystalline MgO. The two phases, one with lattice fringes and the other without any fringe, can be seen in HR-TEM, representing MgO and SiO_2 phases of **MSNT**.⁵¹ The interplanar distances, calculated from the SAED pattern, at 0.391, 0.230, 0.184, 0.147, and 0.126 nm correspond to amorphous SiO_2 , (111), (200), (220), and (222) diffraction planes of MgO cubic structure, respectively. The results obtained from the HR-TEM and SAED pattern are well consistent with the PXRD pattern of pristine MgO.

The textural properties of MgO, **MS**, **MSN**, and **MSNT** were investigated using N_2 adsorption/desorption isotherms at 77 K. The obtained BET specific surface areas and BJH pore size parameters are tabulated in Table S2. According to the IUPAC classification, the adsorption/desorption isotherms of all samples (Figure 4) display type IV behavior with H3 type hysteresis in the relative pressure range $0.1 < P/P_0 < 1$, which indicates the characteristic mesoporous structures with slit-like pores.^{43,52} In the case of **MS**, the isotherm shows an unclosed

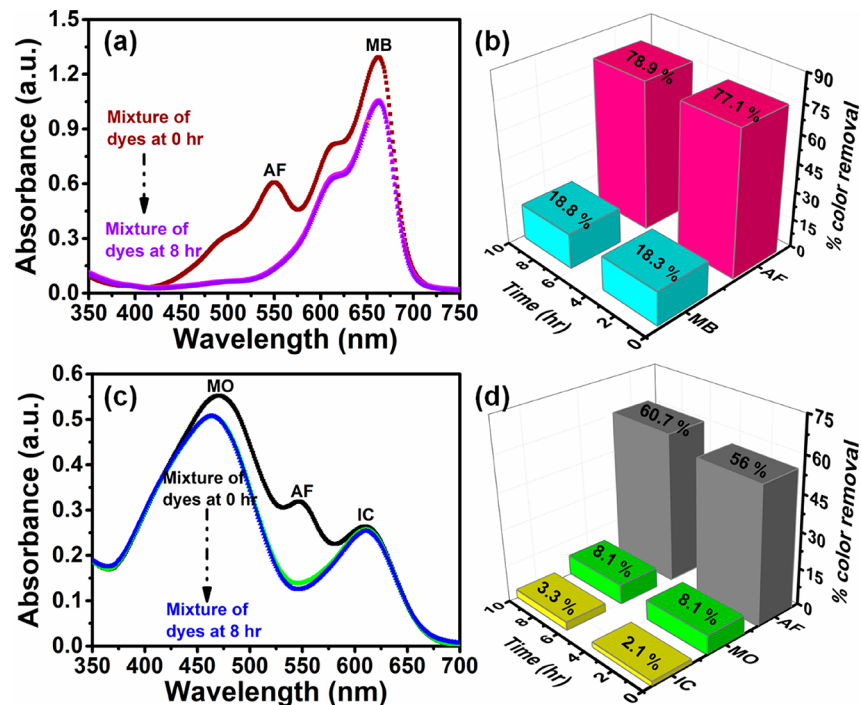


Figure 5. Selective removal capability of MSNT toward (a) mixtures of cationic and anionic dyes (MB + AF) and (c) mixtures of different anionic dyes (MO + IC + AF) and (b, d) corresponding color removal percentage with time.

hysteresis loop even at lower relative pressure, which is perhaps due to the ink-bottle like pores present in MS, restricting the complete removal of N_2 .⁵³ The BET surface area of MgO was found to be $60.14\text{ m}^2/\text{g}$, which after SiO_2 functionalization increases to $101.76\text{ m}^2/\text{g}$ in MS. This significant increase in the surface area suggests the highly porous nature of SiO_2 covering the MgO surface.⁵⁴ The successive functionalization of MS with TEPSIC and aminotetrazole for the syntheses of MSN and MSNT again leads to an abrupt decrease in their surface areas ($65.10\text{ m}^2/\text{g}$ for MSN and $58.99\text{ m}^2/\text{g}$ for MSNT), indicating clogging of pores by the incoming surface functionalities. The BJH pore size distribution, shown in the inset of Figure 4, exhibits the bimodal pore size distribution for all the materials with narrow mesopores and broad macropores distribution. This confirms that the mesoporous character of the materials remains intact even after the functionalization with the organic moieties. Despite having a high surface area, the reduced pore diameter in MS (3.42 nm) compared to that in MgO (17.65 nm) corroborates a higher pore density in MS than MgO.^{54,55} However, compared to MS, similar pore diameters for MSN (3.41 nm) and MSNT (3.77 nm) were observed.

3.2. Dye Removal Studies. Selective removal of a specific dye among several dyes is considered to be an essential parameter in dye removal applications. In this regard, we investigated the dye adsorption capability of 5 mg of MSNT from two 50 mL aqueous solutions containing (Figure S3): (i) mixture of equal concentration (20 mg/L) of an anionic dye acid fuchsin (AF) and a cationic dye methylene blue (MB), (ii) mixture of equal concentration (20 mg/L) of three anionic dyes AF, methyl orange (MO), and indigo carmine (IC). The molecular structures of all the dyes used in this study are shown in Table S3. The percentage color removal of the two solutions, evaluated at different time intervals by UV-vis spectroscopy, is given in Figure 5. Figure 5a shows, in the case

of the solution containing AF and MB dyes, MSNT almost completely vanishes the absorption peak intensity (545 nm) corresponding to AF dye (78.9% color removal, Figure 5b) in 8 h. In contrast, only a slight decrease in the absorption peak intensity (662 nm) of MB (18.8% color removal, Figure 5b) was observed within the same period. In the second case (Figure 5c), for the solution containing a mixture of AF, MO, and IC, selective adsorption of only AF dye was observed. However, characteristic absorption peaks of MO (471 nm) and IC (610 nm) show only a slight reduction in their intensities, corresponding to insignificant color removal of 8.1% and 3.35%, respectively. Collectively, the above observations indicate that MSNT not only exhibits adsorption preference to anionic dye but among the anionic dyes selectively adsorbs AF dye.

The selective adsorption of AF dye in the binary and ternary systems can be attributed to molecular weights and charges of different dyes. In the binary system containing a mixture of anionic and cationic dyes (AF + MB), the anionic AF dye is selectively adsorbed on the MSNT surface because of the dominating electrostatic attraction between positively charged MSNT and negatively charged AF dye. In the case of ternary systems containing three anionic dyes (AF + IC + MO), the preferential adsorption of AF dye on MSNT may be attributed to its higher molecular weight^{56,57} and the presence of more number of anionic groups ($-\text{SO}_3^-$) compared to IC and MO dyes. Further, to confirm the adsorption of AF dye on the surface of MSNT, the FT-IR spectrum of AF adsorbed MSNT was recorded and compared with that of pristine MSNT and AF (Figure S4). The FT-IR spectrum of the AF adsorbed MSNT sample shows additional peaks at 1023, 1093, and 1190 cm^{-1} , which are related to vibrations of $\text{S}=\text{O}$ groups present in AF dye,⁵⁸ and thus confirms the adsorption of AF on MSNT surface.

The pH-dependent adsorption study is an important investigation to understand the adsorption mechanism and possible interactions between adsorbent and adsorbate. Therefore, we investigated the percentage color removal ability of MSNT for AF dye at different pH in the range 3–9 (Figure 6b). The highest color removal percentage of 97% was

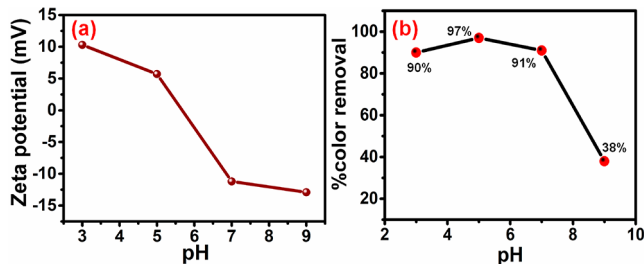


Figure 6. (a) ζ potential of MSNT as a function of pH and (b) effect of pH on AF dye adsorption onto MSNT.

observed between pH 5.0 and pH 6.0. It can be rationalized as, under acidic pH, the positively charged MSNT surface, resulting from the protonation of its amine groups, is expected to attract the anionic AF dye due to the strong electrostatic interaction.¹² The relatively low adsorption (90% color removal) at pH 3 can be attributed to the fact that under very strong acidic conditions, the sulfonate groups of AF start reprototonating, reducing the anionic character of the dye. When the pH increases toward the alkaline side (pH = 7–9), the color removal efficiency of MSNT is drastically reduced due to the deprotonation of its surface ammonium groups. Addition-

ally, the hydroxyl (OH^-) ions combined with adsorption sites and lead to the formation of a negative charge on the surface of MSNT, which repels the negatively charged AF dye.⁴ Further to confirm the surface charge of MSNT, ζ potential measurement of MSNT was carried out in different aqueous suspensions in the pH range 3–9 (Figure 6a). The study shows that below the isoelectric point (IEP, pH 5.8), MSNT exhibits a positive surface potential, facilitating the anionic AF adsorption. However, at higher pH, due to the negative ζ potential of MSNT, the adsorption is drastically reduced.⁴ From Figure 6b, it can be clearly seen that, even after isoelectric point (pH 5.8), there is no significant reduction in color removal percentage until pH 7. Such an observation corroborates that, besides electrostatic interaction between AF and MSNT, H-bonding is also an important interaction during the adsorption process.^{57,59} The possible ways of H-bonding between MSNT and AF dye are depicted in Scheme S1.

To calculate the dye adsorption capacity of MSNT and to understand the adsorption behavior, adsorption of varying concentrations of AF dye (20, 40, 60, 80, 100, 120, 150 mg/L) was studied on the MSNT surface. Figure 7a depicts the change in equilibrium adsorption capacity (C_e) with the increase in initial dye concentration. With the increase in dye concentration, the equilibrium adsorption capacity increased from 66.5 mg/g for 20 mg/L dye solution to a value of 775.6 mg/g for the highest studied dye concentration, 150 mg/L. Such observation of a continuous increase in adsorption capacity with the increasing concentration of dye can be explained by the fact that the rising dye concentration enhances the concentration gradient between aqueous and

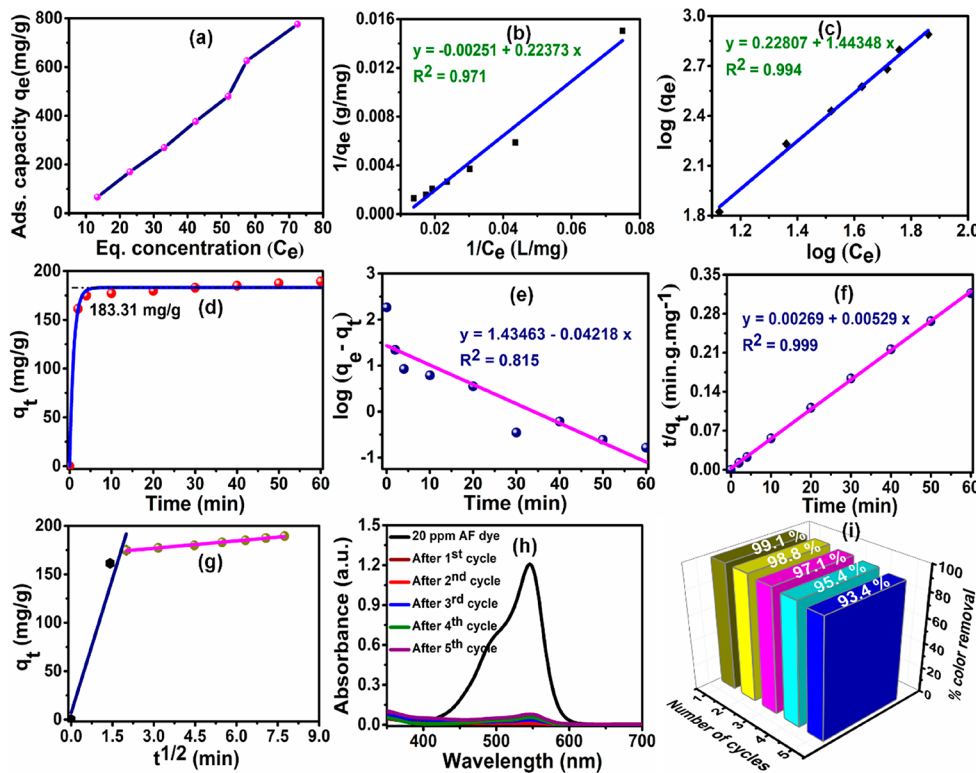


Figure 7. (a) Equilibrium adsorption isotherm of AF dye with different initial concentration, (b) Langmuir isotherm model, (c) Freundlich isotherm model, (d) experimental adsorption capacity at time t , (e) pseudo-first-order kinetic model, (f) pseudo-second-order kinetic model, (g) intraparticle diffusion kinetic model of the adsorption process, (h) UV-vis spectra of AF dye solution after each cycle, and (i) corresponding color removal percentages.

solid adsorbent phase, which drives the diffusion of dye molecules toward MSNT surface and, thereby, continuously increases the adsorption capacity.^{3,60} A comparison of adsorption capacities of different amine-based adsorbents with that of the present MSNT material is given in Table S4, which shows that the adsorption capacity of MSNT for AF is much higher compared to the previously explored materials. Such a high dye adsorption capacity of MSNT can be attributed to aminotetrazole and carbamide surface functionalities, which facilitate the stronger anchorage of AF onto the surface of MSNT via the formation of several H-bonds,^{7,61} besides electrostatic interactions, in their protonated form. The role of aminotetrazole surface functionality was also understood by comparing the color removal percentages by MSNT and MS (Figure S5). The MSNT, having aminotetrazole, shows 96% color removal of AF dye, whereas only 80% color removal was observed by MS.

To understand the dye adsorption process, the suitability of Langmuir and Freundlich adsorption models was ascertained by fitting experimental adsorption data in both the models. Langmuir adsorption isotherm suggests that the adsorption of dye molecules on the adsorbent surface is homogeneous and proceeds via monolayer formation. The linearized form of the Langmuir isotherm is expressed in eq 5.^{60–62}

$$\frac{1}{q_e} = \frac{1}{q_{\max}} + \frac{1}{q_{\max} K_L} \frac{1}{C_e} \quad (5)$$

where C_e and q_e (mg/L) are equilibrium concentration of aqueous dye solutions and the equilibrium adsorption capacity; q_{\max} (mg/g) is the maximum adsorption capacity; and K_L (L/mg) is Langmuir constant, which is related to the energy of adsorption. The Langmuir adsorption isotherm model, showing a linear relation between $1/C_e$ and $1/q_e$ with regression factor value (R^2) 0.971, is given in Figure 7b. The values of other parameters (K_L , slope, and intercept) are given in Table S5. The feasibility of the adsorption process was also evaluated by calculating the dimensionless separation factor (R_L) using eq 6.⁶³

$$R_L = \frac{1}{1 + K_L C_0} \quad (6)$$

where C_0 is the initial dye concentration. The calculated values of the R_L were found in the range 0.816–0.373 for different initial dye concentrations of 20–150 mg/L, which indicated a favorable adsorption process.⁶³

Freundlich adsorption isotherm model proposes a heterogeneous multilayer adsorption process and is expressed using eq 7.⁶²

$$\log q_e = \log K_F + \frac{1}{n} \log C_e \quad (7)$$

where K_F (L·g⁻¹) and n are the Freundlich constant and heterogeneity factor, respectively. Figure 7c shows the isotherm model following a linear correlation between $\log q_e$ and $\log C_e$ with a regression factor (R^2) value 0.994. The value of n^{-1} can be determined by calculating the slope of the linear graph, whose different values <1 or ≈1 or >1, indicate the adsorption process to be favorable or linear or unfavorable, respectively. The calculated n^{-1} for Freundlich isotherm was found to be 0.693, indicating a favorable adsorption process. Though values of separation factor ($R_L = 0.816$) and heterogeneity factor ($n^{-1} = 0.693$) suggest the favorability of

both the models, the higher R^2 value for Freundlich isotherm (0.994) compared to that of Langmuir (0.971) indicates that the Freundlich is preferred over the Langmuir adsorption model.

Adsorption kinetics was studied to understand the adsorption mechanism and the factors involved in determining the rate of the adsorption. In general, the rate of adsorption depends on the contact time (t) of aqueous dye solutions with the adsorbent surface and also on the diffusion process. To understand the kinetics, the adsorption of AF dye solution was studied on the MSNT surface at different time intervals (Figure 7d), and the corresponding data were fitted in pseudo-first-order and pseudo-second-order kinetic models.

The pseudo-first-order kinetic model can be expressed by eq 8.^{42,64}

$$\log(q_e - q_t) = \log q_e - \frac{k_1 t}{2.303} \quad (8)$$

where q_t , q_e , and k_1 are the amount of dye adsorbed at different time intervals (t in min), equilibrium adsorption capacity, and pseudo-first-order rate constant (min⁻¹), respectively. The linear graph between $\log(q_e - q_t)$ vs contact time t is depicted in Figure 7e, which shows a linear regression value of 0.815. The q_e and k_1 values of the linear graph, obtained from intercept and slope, are given Table S6.

The linear expression for the pseudo-second-order kinetic model is given in eq 9.

$$\frac{t}{q_t} = \frac{1}{k_2 q_e^2} + \frac{t}{q_e} \quad (9)$$

where k_2 is the rate constant for the pseudo-second-order kinetics, whereas other parameters are the same as mentioned in eq 8. The graphical form of eq 9 is shown in Figure 7f, in which the linear correlation of t/q_t and t almost fits with the experimental data with an R^2 value of 0.999. The other parameters of the equation (k_2 and q_e) are tabulated in Table S6. From Figure 7e and Figure 7f, the observed R^2 value (0.999) for pseudo-second-order is almost close to unity and thus suggests that the adsorption of AF on to the surface of MSNT follows the pseudo-second-order kinetics. Moreover, the close agreement between calculated and experimental q_e values ($q_{e(\text{cal})} = 189.03$ mg/g and $q_{e(\text{exp})} = 183.31$ mg/g) also confirms that the adsorption process follows pseudo-second-order model.

The extent of the percentage color removal of aqueous AF dye solution by MSNT was also studied with increasing time. The corresponding time-dependent UV-vis spectra and the color removal bar diagram are shown in Figure S6. The color removal bar diagram indicates rapid initial dye adsorption (78.6% color removal within 2 min), which subsequently slows down and reaches 92.8% in 60 min. The same pattern can also be seen in Figure 7d, where maximum equilibrium adsorption (q_e) 183.31 mg/g is achieved in 5 min, and the adsorption curve gets flattened with a further increase in adsorption time.

To further understand the factors responsible for such type of adsorption behavior, surface diffusion model analysis was performed. An adsorption process is accompanied mainly in three steps: (i) diffusion of adsorbate from the bulk phase to the adsorbent boundary layer, (ii) diffusion of adsorbate from the boundary layer to the adsorbent surface, and finally (iii) intraparticle diffusion of adsorbate into the available pores of the adsorbent. The involvement of the above steps in

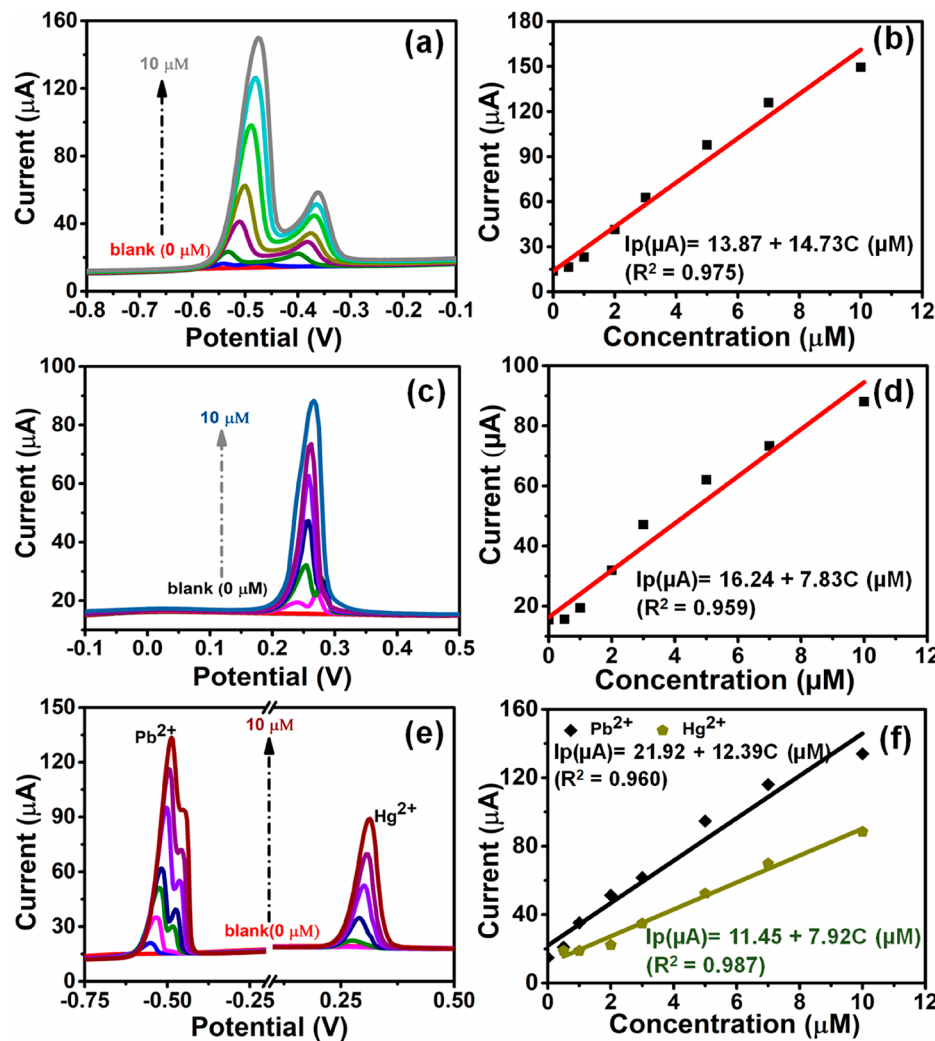


Figure 8. Electrochemical responses of MSNT toward the individual (a, c) Pb(II) and Hg(II) ions and their corresponding calibration plot (b, d) Pb(II) and Hg(II). (e) Simultaneous detection of Pb(II) and Hg(II) ions. (f) Corresponding calibration plots.

determining the rate of adsorption can be understood by the intraparticle kinetic model, developed by Weber and Morris, which is given in eq 10.^{64,65}

$$q_t = k_i t^{0.5} + C \quad (10)$$

where k_i is the intraparticle diffusion rate constant and the intercept C represents the boundary layer thickness, respectively. The q_t vs $t^{1/2}$ graph (Figure 7g) shows two linear segments, corresponding to diffusion of AF dye from the boundary layer to the MSNT surface and subsequent intraparticle diffusion of the surface diffused AF into the pores of MSNT. The corresponding k_i and C for both segments are tabulated in Table S6. Figure 7g shows that the first segment passes through the origin, which indicates that the step involving diffusion of AF from the aqueous phase to the MSNT boundary has an insignificant role in determining the rate of the adsorption, which is understandable as the adsorption was carried out under shaking condition. The lower value of diffusion rate constant for the second segment ($k_{i2} = 2.55 \text{ mg}\cdot\text{g}^{-1}\cdot\text{min}^{-1/2}$) than that of the first segment ($k_{i1} = 6.96 \text{ mg}\cdot\text{g}^{-1}\cdot\text{min}^{-1/2}$) clearly indicates that the intraparticle diffusion of AF dye molecules into the pores of MSNT is the rate-determining step for the adsorption.^{42,64}

The recyclable feature of a material is an important criterion for its practical application; therefore, we also studied the adsorption–desorption cycle of our material to understand its reusability. To check the reusability of the material, five cycles of the adsorption–desorption studies were performed using an aqueous NaCl solution as eluent. The smaller size of Cl⁻ anions facilitate the desorption of surface adsorbed AF molecules through chloride–sulfonate ion exchange.⁷ The UV-vis spectrum of the filtrate from each cycle and corresponding percentage color removal are given in Figure 7h and Figure 7i. From Figure 7i, it is evident that, until five cycles, the percentage color removal ability of the material drops only by 5.7%, indicating the robust behavior of the material for the practical application. The digital photograph of the adsorption–desorption experiment is given in Figure S7.

3.3. Electrochemical Detection of Heavy Metal Ions (Pb(II) and Hg(II)). The well-established fact of deriving superior electrochemical sensing performance by impregnation or surface modification of materials with nitrogen-rich moieties prompted us to explore the electrochemical stripping response on MSNT modified GCE (GC-MSNT). For comparison purposes, the stripping responses of the bare GC, GC-MgO, GC-MS, and GC-MSNT electrodes were examined for 20 μM aqueous solutions of Pb(II) and Hg(II) metal ions. Figure S8

shows the SWASV spectra of different electrodes, which displays two current peaks at potentials -0.54 V and $+0.25$ V for the oxidations of Pb and Hg, respectively. Among the four electrodes investigated, the GC-MSNT electrode showed the highest stripping current response compared to other electrodes. This can be attributed to the strong chelating effect of carbamide and tetrazole functionalities of MSNT with Pb(II) and Hg(II) metal ions. Consequently, further studies were carried out for Pb(II) and Hg(II) using the MSNT modified electrode. The possible interactions between MSNT and metal ions and the sensing mechanism are depicted and discussed in Scheme S2.

The electroanalytical response of the individual metal ion was studied using GC-MSNT under the standard conditions mentioned in the experimental section. Figure 8a shows the change in stripping current, corresponding to Pb oxidation at -0.54 V, with increasing concentration of Pb(II) ions in the range $0.5 \mu\text{M}$ to $10 \mu\text{M}$. As depicted in Figure 8b, the Pb stripping current rises linearly with increase in Pb(II) concentration, following a linear equation $I_p = 13.87 + 14.73C$ (where I_p in μA and C in μM are stripping current and metal ion concentration, respectively) with a regression factor value close to 1 ($R^2 = 0.975$). The detection limit (LOD) and sensitivity, calculated from the linear equation, were found to be $0.019 \mu\text{M}$ (3σ method)^{30,66} and $75 \mu\text{A}\cdot\mu\text{M}^{-1}\cdot\text{cm}^{-2}$, respectively.

The stripping current response of GC-MSNT for individual Hg oxidation was also investigated under the same concentration range of Hg(II) ions (Figure 8c). The linear dependence of stripping current with the changing concentration of Hg(II) ion is shown in Figure 8d with the equation $I_p = 16.24 + 7.83C$ (I_p and C have the same meanings and units as mentioned before) having an R^2 value of 0.959. By use of this equation, the calculated LOD and sensitivity for Hg(II) were found to be $0.041 \mu\text{M}$ and $39.89 \mu\text{A}\cdot\mu\text{M}^{-1}\cdot\text{cm}^{-2}$, respectively. It should be mentioned here that with increasing metal ion concentration, a slight anodic shift in the peak potentials for the oxidations of both metal ions was observed. It can be ascribed to the fact that the increasing concentration of metal ions causes higher metal deposition on the electrode, which, during stripping, shifts the equilibrium toward positive potential.^{67,68} The comparative performance of the present material with that of earlier reported amine-modified materials toward the Pb(II) and Hg(II) detection is summarized in Table S7. It is evident from the table that the MSNT, in most cases, shows better performance with an acceptable linear range of detection and therefore can be employed for real-time monitoring.

The well-separated oxidation peaks of Pb and Hg offer an opportunity to investigate the simultaneous detection of the two ions from the same solution. Therefore, we also attempted to study the stripping current response of MSNT for the aqueous solutions containing equimolar Pb(II) and Hg(II) ions (concentration range $0.5 \mu\text{M}$ to $10 \mu\text{M}$) (Figure 8e). As can be seen in Figure 8e, the coexistence of Pb(II) and Hg(II) ions in the solution does not mutually alter their oxidation potentials. The observed stripping current peaks are clearly distinguishable, which confirms the prospect of GC-MSNT electrode for simultaneous detection of Pb(II) and Hg(II) ions. Figure 8f shows linear fitting curves for change in stripping currents for Pb and Hg oxidations with an increasing concentration of ions. The obtained linear equations corresponding to both lines are (i) $I_p = 21.92 + 12.39C$ (R^2

= 0.96) for Pb(II) and (ii) $I_p = 11.45 + 7.92C$ ($R^2 = 0.987$) for Hg(II). The calculated LODs and sensitivities during the simultaneous detection were found to be $0.0145 \mu\text{M}$ and $63.13 \mu\text{A}\cdot\mu\text{M}^{-1}\cdot\text{cm}^{-2}$, respectively, for Pb(II) and $0.0141 \mu\text{M}$ and $40.35 \mu\text{A}\cdot\mu\text{M}^{-1}\cdot\text{cm}^{-2}$, respectively, for Hg(II). Moreover, in simultaneous detection, the additional shoulder peak in the Pb(II) compared to its individual detection can be attributed to the effect of Pb–Hg interaction during the stripping process.^{10,69}

For a sensor to be reliable, its performance should not be altered by the presence of other species. Therefore, we also performed the interference study by investigating the sensing ability of our material in the presence of an excess of different metal ions. In this study, the percentage change in stripping current on GC-MSNT for standard solutions of Pb(II) and Hg(II) ions ($20 \mu\text{M}$ solutions of Pb(II) and Hg(II) in $0.1 \text{ M NaAC-HAc buffer}$) was recorded after addition of 10-fold excess of interfering ions, such as Na(I), K(I), Ca(II), Ni(II), Co(II), Cd(II), Cu(II), and Fe(III). The percentage change in anodic current for Pb and Hg corresponding to each interfering ions is given in Table S8. Table S8 suggests that, compared to the Pb oxidation, the oxidation of Hg is more sensitive to the interfering ions, resulting in a comparatively higher deviation in the stripping current due to the intermetallic compound formation. The maximum percentage current change for Hg oxidation was only 8.18% in the presence of Na^+ ion, which is considered to be no apparent interference in the detection process.^{10,70} This confirms the selective affinity of MSNT for Pb(II) and Hg(II) ions without any interference in its stripping current response from other metal ions.⁹

Repeatability and reproducibility are critical factors for ensuring the precision of the electrode materials for heavy metal ion sensing. The repeatability of the MSNT modified GC electrode was done by conducting repeated SWASV measurements (15 times) of standard solutions of Pb(II) and Hg(II) ions. The result showed that each cycle gave almost the same peak current value, and the calculated relative standard deviations (RSDs) were found to be 1.78% and 1.88% for Pb(II) and Hg(II) ions, respectively (Figure S9). We also evaluated the reproducibility of the material by measuring the stripping current on two different electrodes coated with MSNT (Figure S10). The RSDs of resultant current peaks from two electrodes were calculated to be 2.52% and 2.01% for Pb(II) and Hg(II) ions, respectively. Finally, the stability of the GC-MSNT electrode was investigated by comparing the stripping current response of the freshly fabricated electrode with that of a GC-MSNT electrode exposed in the air for 7 days at room temperature (Figure S11). The observed RSDs in their stripping currents were found to be 0.66% and 3.61% for Pb(II) and Hg(II) ions, respectively. The repeatability, reproducibility, and stability studies collectively corroborate the robust and precise character of the present electrode material for a practical application in electrochemical sensing of Pb(II) and Hg(II) ions.

In addition to the above studies, the feasibility of the proposed sensing system was also investigated for real-time tap and pond water samples (both samples were collected from the local body) for the determination of the Pb(II) and Hg(II) ions. The calculated average percentage recoveries for both real-time samples were in an acceptable range, which have been summarized in Table S9 along with the mean concentrations and relative standard deviations (RSDs). The

% recoveries of the Pb(II) and Hg(II) were found in the range between 95% and 117%, and the obtained RSD values are less than 4%, which indicate the potential applicability of MSNT in the real-time sample analysis.

4. CONCLUSION

A tetrazole functionalized MgO–SiO₂ nanocomposite (MSNT) has been synthesized and successfully applied for the removal of toxic dye and sensitive detection of heavy metal ions. In dye removal application, the nanomaterial exhibits rapid and selective adsorption of acid fuchsin dye with a high adsorption capacity (775.6 mg/g), which in most cases is superior to the earlier reported amine-based absorbents. The detailed adsorption mechanism and kinetic studies indicate that the dye adsorption takes place by the Freundlich model, following pseudo-second-order kinetics, where intraparticle diffusion on the surface of the material is the rate-determining step. The synthesized nanocomposite can be reused in multiple cycles without any appreciable loss in its performance, signifying its strong stability. MSNT has also been investigated as an electrode material for the detection of heavy metal ions Pb(II) and Hg(II). The modification of the GC electrode with the material significantly boosts the stripping current and, thereby, leads to excellent LOD (19 nM for Pb(II) and 41 nM for Hg(II)) and sensitivity (\approx 75 $\mu\text{A}\cdot\mu\text{M}^{-1}\cdot\text{cm}^{-2}$ for Pb(II) and 40 $\mu\text{A}\cdot\mu\text{M}^{-1}\cdot\text{cm}^{-2}$). Further, to establish the practical applicability of the material, other studies such as simultaneous detection, real-time sample analysis, repeatability, stability, and the effect of interfering ions are also performed. These investigations strongly corroborate that the new material reported in this article can be a promising adsorbent for effective removal of AF dye, and an electrode material for sensitive electrochemical detection of a trace of Pb(II) and Hg(II) ions from the aqueous system.

■ ASSOCIATED CONTENT

Supporting Information

The Supporting Information is available free of charge at <https://pubs.acs.org/doi/10.1021/acsanm.0c02351>.

EDX spectra of MgO, MS, and MSNT, elemental mapping of MSNT, digital images of selectivity studies, the molecular structures of dyes, FTIR spectra of MSNT before and after dye adsorption, dye adsorption mechanism, UV-vis spectra and color removal bar chart of AF dye with respect to time, digital photographs of recyclability studies, SWASV curves of different electrodes, HMI sensing mechanism, repeatability, reproducibility, and stability studies of MSNT-GCE, comparison of textural properties of as-prepared adsorbents, comparison table for dye removal and HMI detection, table for real-time sample analysis (PDF)

■ AUTHOR INFORMATION

Corresponding Author

Dhirendra K. Rai — Discipline of Metallurgy Engineering and Materials Science, Indian Institute of Technology Indore, Indore 453552, India;  orcid.org/0000-0003-4917-0839; Phone: +91 731 660 3278; Email: dkrai@iiti.ac.in

Authors

Sarathkumar Krishnan — Discipline of Metallurgy Engineering and Materials Science, Indian Institute of Technology Indore, Indore 453552, India;  orcid.org/0000-0003-0201-5102

Sobhan Chatterjee — Discipline of Chemistry, Indian Institute of Technology Indore, Indore 453552, India

Ankit Solanki — Discipline of Metallurgy Engineering and Materials Science, Indian Institute of Technology Indore, Indore 453552, India

Nikita Guha — Discipline of Metallurgy Engineering and Materials Science, Indian Institute of Technology Indore, Indore 453552, India

Mayank K. Singh — Discipline of Metallurgy Engineering and Materials Science, Indian Institute of Technology Indore, Indore 453552, India

Anoop K. Gupta — Discipline of Chemistry, Indian Institute of Technology Indore, Indore 453552, India

Complete contact information is available at:

<https://pubs.acs.org/10.1021/acsanm.0c02351>

Notes

The authors declare no competing financial interest.

■ ACKNOWLEDGMENTS

D.K.R. acknowledges DST-SERB, New Delhi, for financial support (Project YSS/2015/000034). S.K., A.S., N.G., M.K.S., and A.K.G thank IIT Indore for their research fellowships. All authors thank Sophisticated Instrument Center, IIT Indore, and Materials Research Center, MNIT Jaipur, for the instrumentation facilities. All authors thank Dr. Senthilkumaran for the ζ potential measurements.

■ DEDICATION

This work is dedicated to Professor Pradeep Mathur, IIT Bombay, India, on his 65th birthday.

■ REFERENCES

- (1) Zhang, Y. N.; Niu, Q.; Gu, X.; Yang, N.; Zhao, G. Recent Progress on Carbon Nanomaterials for the Electrochemical Detection and Removal of Environmental Pollutants. *Nanoscale* **2019**, *11* (25), 11992–12014.
- (2) Deb, A.; Kanmani, M.; Debnath, A.; Bhowmik, K. L.; Saha, B. Ultrasonic Assisted Enhanced Adsorption of Methyl Orange Dye onto Polyaniline Impregnated Zinc Oxide Nanoparticles: Kinetic, Isotherm and Optimization of Process Parameters. *Ultrason. Sonochem.* **2019**, *54*, 290–301.
- (3) Srilakshmi, C.; Saraf, R. Ag-Doped Hydroxyapatite as Efficient Adsorbent for Removal of Congo Red Dye from Aqueous Solution: Synthesis, Kinetic and Equilibrium Adsorption Isotherm Analysis. *Microporous Mesoporous Mater.* **2016**, *219*, 134–144.
- (4) Bhowmik, M.; Debnath, A.; Saha, B. Fabrication of Mixed Phase Calcium Ferrite and Zirconia Nanocomposite for Abatement of Methyl Orange Dye from Aqua Matrix: Optimization of Process Parameters. *Appl. Organomet. Chem.* **2018**, *32* (12), e4607.
- (5) Aragay, G.; Pons, J.; Merkoci, A. Recent Trends in Macro-, Micro-, and Nanomaterial-Based Tools and Strategies for Heavy-Metal Detection. *Chem. Rev.* **2011**, *111* (5), 3433–3458.
- (6) Dong, Z.; Wang, D.; Liu, X.; Pei, X.; Chen, L.; Jin, J. Bio-Inspired Surface-Functionalization of Graphene Oxide for the Adsorption of Organic Dyes and Heavy Metal Ions with a Superhigh Capacity. *J. Mater. Chem. A* **2014**, *2* (14), 5034–5040.
- (7) Cheng, Y.; Feng, Q.; Ren, X.; Yin, M.; Zhou, Y.; Xue, Z. Adsorption and Removal of Sulfonic Dyes from Aqueous Solution onto a Coordination Polymeric Xerogel with Amino Groups. *Colloids Surf., A* **2015**, *485*, 125–135.

- (8) Bhowmik, M.; Debnath, A.; Saha, B. Fabrication of Mixed Phase CaFe₂O₄ and MnFe₂O₄ Magnetic Nanocomposite for Enhanced and Rapid Adsorption of Methyl Orange Dye: Statistical Modeling by Neural Network and Response Surface Methodology. *J. Dispersion Sci. Technol.* **2019**, 1–12.
- (9) Ma, Y.; Wang, Y.; Xie, D.; Gu, Y.; Zhu, X.; Zhang, H.; Wang, G.; Zhang, Y.; Zhao, H. Hierarchical MgFe-Layered Double Hydroxide Microsphere/Graphene Composite for Simultaneous Electrochemical Determination of Trace Pb(II) and Cd(II). *Chem. Eng. J.* **2018**, 347, 953–962.
- (10) Seenivasan, R.; Chang, W.-J.; Gunasekaran, S. Highly Sensitive Detection and Removal of Lead Ions in Water Using Cysteine-Functionalized Graphene Oxide/Polyppyrrole Nanocomposite Film Electrode. *ACS Appl. Mater. Interfaces* **2015**, 7 (29), 15935–15943.
- (11) Deshmukh, M. A.; Celiesiute, R.; Ramanaviciene, A.; Shirsat, M. D.; Ramanavicius, A. EDTA-PANI/SWCNTs Nanocomposite Modified Electrode for Electrochemical Determination of Copper (II), Lead (II) and Mercury (II) Ions. *Electrochim. Acta* **2018**, 259, 930–938.
- (12) Bhowmik, M.; Deb, K.; Debnath, A.; Saha, B. Mixed Phase Fe₂O₃/Mn₃O₄ Magnetic Nanocomposite for Enhanced Adsorption of Methyl Orange Dye: Neural Network Modeling and Response Surface Methodology Optimization. *Appl. Organomet. Chem.* **2018**, 32 (3), e4186.
- (13) Yang, Z.; Zhu, L.; Chen, L. Selective Adsorption and Separation of Dyes from Aqueous Solution by Core-Shell Structured NH₂-Functionalized UiO-66 Magnetic Composites. *J. Colloid Interface Sci.* **2019**, 539, 76–86.
- (14) Lu, M.; Deng, Y.; Luo, Y.; Lv, J.; Li, T.; Xu, J.; Chen, S.-W.; Wang, J. Graphene Aerogel–Metal–Organic Framework-Based Electrochemical Method for Simultaneous Detection of Multiple Heavy-Metal Ions. *Anal. Chem.* **2019**, 91 (1), 888–895.
- (15) Park, S. S.; Ha, C. S. Organic-Inorganic Hybrid Mesoporous Silicas: Functionalization, Pore Size, and Morphology Control. *Chem. Rec.* **2006**, 6 (1), 32–42.
- (16) Zhou, S. F.; Wang, J. J.; Gan, L.; Han, X. J.; Fan, H. L.; Mei, L. Y.; Huang, J.; Liu, Y. Q. Individual and Simultaneous Electrochemical Detection toward Heavy Metal Ions Based on L-Cysteine Modified Mesoporous MnFe₂O₄ Nanocrystal Clusters. *J. Alloys Compd.* **2017**, 721, 492–500.
- (17) Aoopngan, C.; Nonkumwong, J.; Phumying, S.; Promjantuek, W.; Maensiri, S.; Noisa, P.; Pinitsoontorn, S.; Ananta, S.; Srisombat, L. Amine-Functionalized and Hydroxyl-Functionalized Magnesium Ferrite Nanoparticles for Congo Red Adsorption. *ACS Appl. Nano Mater.* **2019**, 2 (8), 5329–5341.
- (18) Wang, F.; Zhang, L.; Wang, Y.; Liu, X.; Rohani, S.; Lu, J. Fe₃O₄@SiO₂@CS-TETA Functionalized Graphene Oxide for the Adsorption of Methylene Blue (MB) and Cu(II). *Appl. Surf. Sci.* **2017**, 420, 970–981.
- (19) Pan, Y.; Wang, J.; Sun, C.; Liu, X.; Zhang, H. Fabrication of Highly Hydrophobic Organic-Inorganic Hybrid Magnetic Polysulfone Microcapsules: A Lab-Scale Feasibility Study for Removal of Oil and Organic Dyes from Environmental Aqueous Samples. *J. Hazard. Mater.* **2016**, 309, 65–76.
- (20) Sim, K.; Lee, N.; Kim, J.; Cho, E.-B.; Gunathilake, C.; Jaroniec, M. CO₂ Adsorption on Amine-Functionalized Periodic Mesoporous Benzenesilicas. *ACS Appl. Mater. Interfaces* **2015**, 7 (12), 6792–6802.
- (21) Xiao, K.; Jiang, D.; Amal, R.; Wang, D. W. A 2D Conductive Organic–Inorganic Hybrid with Extraordinary Volumetric Capacitance at Minimal Swelling. *Adv. Mater.* **2018**, 30 (26), 1800400.
- (22) Hu, M.; Yan, X.; Hu, X.; Zhang, J.; Feng, R.; Zhou, M. Ultra-High Adsorption Capacity of MgO/SiO₂ Composites with Rough Surfaces for Congo Red Removal from Water. *J. Colloid Interface Sci.* **2018**, 510, 111–117.
- (23) Yue, Y.; Peng, Z.; Wang, W.; Cai, Y.; Tan, F.; Wang, X.; Qiao, X. Facile Preparation of MgO-Loaded SiO₂ Nanocomposites for Tetracycline Removal from Aqueous Solution. *Powder Technol.* **2019**, 347, 1–9.
- (24) Xiong, S.; Ye, S.; Hu, X.; Xie, F. Electrochemical Detection of Ultra-Trace Cu(II) and Interaction Mechanism Analysis Between Amine-Groups Functionalized CoFe₂O₄/Reduced Graphene Oxide Composites and Metal Ion. *Electrochim. Acta* **2016**, 217, 24–33.
- (25) Yang, Z.; Yang, Y.; Zhu, X.; Chen, G.; Zhang, W. An Outward Coating Route to CuO/MnO₂ Nanorod Array Films and Their Efficient Catalytic Oxidation of Acid Fuchsin Dye. *Ind. Eng. Chem. Res.* **2014**, 53 (23), 9608–9615.
- (26) Sun, Y. F.; Zhao, L. J.; Jiang, T. J.; Li, S. S.; Yang, M.; Huang, X. J. Sensitive and Selective Electrochemical Detection of Heavy Metal Ions Using Amino-Functionalized Carbon Microspheres. *J. Electroanal. Chem.* **2016**, 760, 143–150.
- (27) Zhu, W.; Liu, L.; Liao, Q.; Chen, X.; Qian, Z.; Shen, J.; Liang, J.; Yao, J. Functionalization of Cellulose with Hyperbranched Polyethylenimine for Selective Dye Adsorption and Separation. *Cellulose* **2016**, 23 (6), 3785–3797.
- (28) Xiong, S.; Wang, M.; Cai, D.; Li, Y.; Gu, N.; Wu, Z. Electrochemical Detection of Pb(II) by Glassy Carbon Electrode Modified with Amine-Functionalized Magnetite Nanoparticles. *Anal. Lett.* **2013**, 46 (6), 912–922.
- (29) Guo, Z.; Li, D.-d.; Luo, X.-k.; Li, Y.-h.; Zhao, Q.-N.; Li, M.-m.; Zhao, Y.-t.; Sun, T.-s.; Ma, C. Simultaneous Determination of Trace Cd(II), Pb(II) and Cu(II) by Differential Pulse Anodic Stripping Voltammetry Using a Reduced Graphene Oxide-Chitosan/Poly-L-Lysine Nanocomposite Modified Glassy Carbon Electrode. *J. Colloid Interface Sci.* **2017**, 490, 11–22.
- (30) Zhou, S.-F.; Han, X.-J.; Liu, Y.-Q. SWASV Performance toward Heavy Metal Ions Based on a High-Activity and Simple Magnetic Chitosan Sensing Nanomaterials. *J. Alloys Compd.* **2016**, 684, 1–7.
- (31) Nasir, T.; Herzog, G.; Hébrant, M.; Despas, C.; Liu, L.; Walcarius, A. Mesoporous Silica Thin Films for Improved Electrochemical Detection of Paraquat. *ACS Sensors* **2018**, 3 (2), 484–493.
- (32) Ge, S.; He, X.; Zhao, J.; Duan, L.; Gu, J.; Zhang, Q.; Geng, W. Removal of Cationic Dyes, Heavy Metal Ions, and CO₂ Capture by Adsorption on Mesoporous Silica HMS. *Water, Air, Soil Pollut.* **2017**, 228, 460.
- (33) Zhang, Z.; Lu, S.; Sha, C.; Xu, D. A Single Thiourea-Appended 1,8-Naphthalimide Chemosensor for Three Heavy Metal Ions: Fe³⁺, Pb²⁺, and Hg²⁺. *Sens. Actuators, B* **2015**, 208, 258–266.
- (34) Zeng, G.; Ye, Z.; He, Y.; Yang, X.; Ma, J.; Shi, H.; Feng, Z. Application of Dopamine-Modified Halloysite Nanotubes/PVDF Blend Membranes for Direct Dyes Removal from Wastewater. *Chem. Eng. J.* **2017**, 323, 572–583.
- (35) Muhammad, R.; Jyoti; Mohanty, P. Nitrogen Enriched Triazine Bridged Mesoporous Organosilicas for CO₂ Capture and Dye Adsorption Applications. *J. Mol. Liq.* **2017**, 248, 127–134.
- (36) Yu, H.; Xiao, P.; Tian, J.; Wang, F.; Yu, J. Phenylamine-Functionalized RGO/TiO₂ Photocatalysts: Spatially Separated Adsorption Sites and Tunable Photocatalytic Selectivity. *ACS Appl. Mater. Interfaces* **2016**, 8 (43), 29470–29477.
- (37) Yan, Q.; Lin, Y.; Wu, P.; Zhao, L.; Cao, L.; Peng, L.; Kong, C.; Chen, L. Designed Synthesis of Functionalized Two-Dimensional Metal–Organic Frameworks with Preferential CO₂ Capture. *ChemPlusChem* **2013**, 78 (1), 86–91.
- (38) Nasrollahzadeh, M.; Sajjadi, M.; Khonakdar, H. A. Synthesis and Characterization of Novel Cu(II) Complex Coated Fe₃O₄@SiO₂ Nanoparticles for Catalytic Performance. *J. Mol. Struct.* **2018**, 1161, 453–463.
- (39) Sinirlioglu, D.; Muftuoglu, A. E.; Bozkurt, A. S-(Methacrylamido)Tetrazole and Vinyl Triazole Based Copolymers as Novel Anhydrous Proton Conducting Membranes. *J. Polym. Res.* **2013**, 20 (9), DOI: 10.1007/s10965-013-0242-1.
- (40) Kokab, T.; Shah, A.; Nisar, J.; Khan, A. M.; Khan, S. B.; Shah, A. H. Tripeptide Derivative-Modified Glassy Carbon Electrode: A Novel Electrochemical Sensor for Sensitive and Selective Detection of Cd²⁺ Ions. *ACS Omega* **2020**, 5 (17), 10123–10132.
- (41) Zha, Q.; Sang, X.; Liu, D.; Wang, D.; Shi, G.; Ni, C. Modification of Hydrophilic Amine-Functionalized Metal-Organic

- Frameworks to Hydrophobic for Dye Adsorption. *J. Solid State Chem.* **2019**, *275*, 23–29.
- (42) Moura, A. L. A.; De Oliveira, L. K.; Ciuffi, K. J.; Molina, E. F. Influence of the Hydrophilic/Hydrophobic Nature of Polyetheramines on the Interaction between Amine-Alcohol-Silicate Hybrids and Anionic Dyes for Effective Water Cleaning. *J. Mater. Chem. A* **2015**, *3* (31), 16020–16032.
- (43) Gao, P.; Tian, X.; Yang, C.; Zhou, Z.; Li, Y.; Wang, Y.; Komarneni, S. Fabrication, Performance and Mechanism of MgO Meso-/Macroporous Nanostructures for Simultaneous Removal of As(III) and F in a Groundwater System. *Environ. Sci.: Nano* **2016**, *3* (6), 1416–1424.
- (44) Tao, J.; Xiong, J.; Jiao, C.; Zhang, D.; Lin, H.; Chen, Y. Hybrid Mesoporous Silica Based on Hyperbranch-Substrate Nanonetwork as Highly Efficient Adsorbent for Water Treatment. *ACS Sustainable Chem. Eng.* **2016**, *4* (1), 60–68.
- (45) Yek, S. M.-G.; Azarifar, D.; Nasrollahzadeh, M.; Bagherzadeh, M.; Shokouhimehr, M. Heterogenized Cu(II) Complex of 5-Aminotetrazole Immobilized on Graphene Oxide Nanosheets as an Efficient Catalyst for Treating Environmental Contaminants. *Sep. Purif. Technol.* **2020**, 247 (February), 116952.
- (46) Zieliński, M.; Czajka, B.; Pietrowski, M.; Tomska-Foralewska, I.; Alwin, E.; Kot, M.; Wojciechowska, M. MgO-MgF₂ System Obtained by Sol-Gel Method as an Immobilizing Agent of the Electrolyte Applied in the High Temperature Cells. *J. Sol-Gel Sci. Technol.* **2017**, *84* (2), 368–374.
- (47) Zheng, X.; Huang, M.; You, Y.; Fu, X.; Liu, Y.; Wen, J. One-Pot Synthesis of Sandwich-like MgO@Carbon with Enhanced Sorption Capacity of Organic Dye. *Chem. Eng. J.* **2018**, *334*, 1399–1409.
- (48) Iravani Kashkouli, K.; Torkzadeh-Mahani, M.; Mosaddegh, E. Synthesis and Characterization of Aminotetrazole-Functionalized Magnetic Chitosan Nanocomposite as a Novel Nanocarrier for Targeted Gene Delivery. *Mater. Sci. Eng., C* **2018**, *89*, 166–174.
- (49) Weng, X.; Bao, Z.; Zhang, Z.; Su, B.; Xing, H.; Yang, Q.; Yang, Y.; Ren, Q. Preparation of Porous Cellulose 3,5-Dimethylphenylcarbamate Hybrid Organosilica Particles for Chromatographic Applications. *J. Mater. Chem. B* **2015**, *3* (4), 620–628.
- (50) Çelik, S. Ü.; Bozkurt, A. Preparation and Proton Conductivity of Acid-Doped 5-Aminotetrazole Functional Poly(Glycidyl Methacrylate). *Eur. Polym. J.* **2008**, *44* (1), 213–218.
- (51) Raevskaya, A. E.; Panasiuk, Y. V.; Stroyuk, O. L.; Kuchmiy, S. Y.; Dzhagan, V. M.; Milekhin, A. G.; Yeryukov, N. A.; Sveshnikova, L. A.; Rodyakina, E. E.; Plyusnin, V. F.; et al. Spectral and Luminescent Properties of ZnO-SiO₂ Core-Shell Nanoparticles with Size-Selected ZnO Cores. *RSC Adv.* **2014**, *4* (108), 63393–63401.
- (52) Dong, X.; Ren, B.; Sun, Z.; Li, C.; Zhang, X.; Kong, M.; Zheng, S.; Dionysiou, D. D. Monodispersed CuFe₂O₄ Nanoparticles Anchored on Natural Kaolinite as Highly Efficient Peroxymonosulfate Catalyst for Bisphenol A Degradation. *Appl. Catal., B* **2019**, *253*, 206–217.
- (53) Jeromenok, J.; Weber, J. Restricted Access: On the Nature of Adsorption/Desorption Hysteresis in Amorphous, Microporous Polymeric Materials. *Langmuir* **2013**, *29* (42), 12982–12989.
- (54) Gui, C. X.; Li, Q. J.; Lv, L. L.; Qu, J.; Wang, Q. Q.; Hao, S. M.; Yu, Z. Z. Core-Shell Structured MgO@mesoporous Silica Spheres for Enhanced Adsorption of Methylene Blue and Lead Ions. *RSC Adv.* **2015**, *5* (26), 20440–20445.
- (55) Guo, X.; Deng, Y.; Gu, D.; Che, R.; Zhao, D. Synthesis and Microwave Absorption of Uniform Hematite Nanoparticles and Their Core-Shell Mesoporous Silica Nanocomposites. *J. Mater. Chem.* **2009**, *19* (37), 6706–6712.
- (56) Sarkar, A. K.; Saha, A.; Tarafder, A.; Panda, A. B.; Pal, S. Efficient Removal of Toxic Dyes via Simultaneous Adsorption and Solar Light Driven Photodegradation Using Recyclable Functionalized Amylopectin-TiO₂ – Au Nanocomposite. *ACS Sustainable Chem. Eng.* **2016**, *4* (3), 1679–1688.
- (57) Zhang, F.; Chen, X.; Wu, F.; Ji, Y. High Adsorption Capability and Selectivity of ZnO Nanoparticles for Dye Removal. *Colloids Surf., A* **2016**, *509*, 474–483.
- (58) Hussein, M. Z. b.; Yahaya, A. H.; Shamsul, M.; Salleh, H. M.; Yap, T.; Kiu, J. Acid Fuchsin-Interleaved Mg-Al-Layered Double Hydroxide for the Formation of an Organic-Inorganic Hybrid Nanocomposite. *Mater. Lett.* **2004**, *58* (3–4), 329–332.
- (59) Li, J.; Ng, D. H. L.; Song, P.; Song, Y.; Kong, C. Bio-Inspired Synthesis and Characterization of Mesoporous ZnFe₂O₄ Hollow Fibers with Enhancement of Adsorption Capacity for Acid Dye. *J. Ind. Eng. Chem.* **2015**, *23*, 290–298.
- (60) Zhao, J.; Huang, Q.; Liu, M.; Dai, Y.; Chen, J.; Huang, H.; Wen, Y.; Zhu, X.; Zhang, X.; Wei, Y. Synthesis of Functionalized MgAl-Layered Double Hydroxides via Modified Mussel Inspired Chemistry and Their Application in Organic Dye Adsorption. *J. Colloid Interface Sci.* **2017**, *505*, 168–177.
- (61) Chen, F.; Zhao, E.; Kim, T.; Wang, J.; Hableel, G.; Reardon, P. J. T.; Ananthkrishna, S. J.; Wang, T.; Arconada-Alvarez, S.; Knowles, J. C.; et al. Organosilica Nanoparticles with an Intrinsic Secondary Amine: An Efficient and Reusable Adsorbent for Dyes. *ACS Appl. Mater. Interfaces* **2017**, *9* (18), 15566–15576.
- (62) Chatterjee, S.; Guha, N.; Krishnan, S.; Singh, A. K.; Mathur, P.; Rai, D. K. Selective and Recyclable Congo Red Dye Adsorption by Spherical Fe₃O₄ Nanoparticles Functionalized with 1,2,4,5-Benzene-tetracarboxylic Acid. *Sci. Rep.* **2020**, *10* (1), 111.
- (63) Jena, K. K.; Mittal, H.; Wadi, V. S.; Mani, G. K.; Alhassan, S. M. Advanced TiO₂-SiO₂-Sulfur (Ti-Si-S) Nanohybrid Materials: Potential Adsorbent for the Remediation of Contaminated Wastewater. *ACS Appl. Mater. Interfaces* **2019**, *11* (33), 30247–30258.
- (64) Wang, X.; Hou, C.; Qiu, W.; Ke, Y.; Xu, Q.; Liu, X. Y.; Lin, Y. Protein-Directed Synthesis of Bifunctional Adsorbent-Catalytic Hemin-Graphene Nanosheets for Highly Efficient Removal of Dye Pollutants via Synergistic Adsorption and Degradation. *ACS Appl. Mater. Interfaces* **2017**, *9* (1), 684–692.
- (65) Wu, Y.; Zhang, M.; Zhao, H.; Yang, S.; Arkin, A. Functionalized Mesoporous Silica Material and Anionic Dye Adsorption: MCM-41 Incorporated with Amine Groups for Competitive Adsorption of Acid Fuchsin and Acid Orange II. *RSC Adv.* **2014**, *4* (106), 61256–61267.
- (66) Xu, Z.; Fan, X.; Ma, Q.; Tang, B.; Lu, Z.; Zhang, J.; Mo, G.; Ye, J.; Ye, J. A Sensitive Electrochemical Sensor for Simultaneous Voltammetric Sensing of Cadmium and Lead Based on Fe₃O₄/Multiwalled Carbon Nanotube/Laser Scribed Graphene Composites Functionalized with Chitosan Modified Electrode. *Mater. Chem. Phys.* **2019**, *238*, 121877.
- (67) Kumar, R.; Bhuvana, T.; Sharma, A. Nickel Tungstate-Graphene Nanocomposite for Simultaneous Electrochemical Detection of Heavy Metal Ions with Application to Complex Aqueous Media. *RSC Adv.* **2017**, *7* (67), 42146–42158.
- (68) Yu, X. Y.; Meng, Q. Q.; Luo, T.; Jia, Y.; Sun, B.; Li, Q. X.; Liu, J. H.; Huang, X. J. Facet-Dependent Electrochemical Properties of Co₃O₄ Nanocrystals toward Heavy Metal Ions. *Sci. Rep.* **2013**, *3* (111), 2886.
- (69) Zhai, Z.; Huang, N.; Zhuang, H.; Liu, L.; Yang, B.; Wang, C.; Gai, Z.; Guo, F.; Li, Z.; Jiang, X. A Diamond/Graphite Nanoplatelets Electrode for Anodic Stripping Voltammetric Trace Determination of Zn (II), Cd (II), Pb (II) and Cu (II). *Appl. Surf. Sci.* **2018**, *457*, 1192–1201.
- (70) Li, C.; Zhao, X.; Han, X. Simultaneous Determination of Trace Cd²⁺ and Pb²⁺ Using GR/l-Cysteine/Bi Modified Screen-Printed Electrodes. *Anal. Methods* **2018**, *10* (40), 4945–4950.